organics

MDPI

Article

Adsorption and Electronic Structure of Imidazole-Based Inhibitors on Fe(100): A Combined DFT and DFTB Study

Andrea Navarrete-Mosquera [1], Juan Pedro Palomares-Báez [2], Rody Soto-Rojo [1], Tomás Delgado-Montiel [1], Samuel Soto-Acosta [1], Nora Aydee Sánchez-Bojorge [2], Daniel Glossman-Mitnik [3] and Jesús Baldenebro-López [1,*]

[1] Facultad de Ingeniería Mochis, Universidad Autónoma de Sinaloa, Prol. Ángel Flores y Fuente de Poseidón, S/N, Los Mochis C.P. 81223, Sinaloa, Mexico; andrea.navarrete.fim@uas.edu.mx (A.N.-M.); rody.soto@uas.edu.mx (R.S.-R.); tomas.delgado@uas.edu.mx (T.D.-M.); samuel.soto@uas.edu.mx (S.S.-A.)

[2] Facultad de Ciencias Químicas, Universidad Autónoma de Chihuahua, Campus Universitario #2, Circuito Universitario, Chihuahua C.P. 31125, Chihuahua, Mexico; ppalomares@uach.mx (J.P.P.-B.); nsanchez@uach.mx (N.A.S.-B.)

[3] Laboratorio Virtual NANOCOSMOS, Departamento de Medio Ambiente y Energía, Centro de Investigación en Materiales Avanzados, S. C. Miguel de Cervantes 120, Complejo Industrial Chihuahua, Chihuahua C.P. 31136, Chihuahua, Mexico; daniel.glossman@cimav.edu.mx

* Correspondence: jesus.baldenebro@uas.edu.mx

Abstract

This study presents a theoretical investigation of the adsorption and electronic structure of two imidazole derivatives, 4-(1,4,5-triphenylimidazol-2-yl)-aniline (M1) and *N*,*N*-dimethyl-4-(1,4,5-triphenylimidazol-2-yl)-aniline (M2), on an Fe(100) surface. A combined computational approach, employing Density Functional Theory for molecular reactivity, Density-Functional Tight-Binding for surface interactions, and Molecular Dynamics (MD) simulations for binding stability, was utilized to provide a comprehensive analysis. Quantum–chemical calculations indicate that both inhibitors exhibit strong donor characteristics, with M2 consistently demonstrating greater potential. This enhanced performance is attributed to the strong electron-donating nature and increased structural planarity conferred by the dimethylamine group in M2, which results in a lower HOMO-LUMO energy gap and higher chemical reactivity. Analysis of the inhibitor-surface interaction confirmed a strong electron donor-acceptor mechanism, indicative of stable chemical bond formation and a predominant chemisorption process. MD simulations revealed that both molecules form stable adsorption layers on the iron surface, suggesting initial adsorption behavior.

Keywords: adsorption; imidazole; iron surface; inhibitor; corrosion; DFT; DFTB

Academic Editors: Pan-Pan Zhou and Michal Szostak

Received: 11 March 2026
Revised: 15 May 2026
Accepted: 20 May 2026
Published: 25 May 2026

1. Introduction

Corrosion is an electrochemical process in which metals react with oxygen and other environmental agents [1]. Many industrial systems are composed of metallic surfaces and are particularly vulnerable to corrosion [2]. This process has a significant negative impact on the industries worldwide, leading to estimated annual economic losses of approximately $2.5 trillion USD, equivalent to about 3.4% of the global Gross Domestic Product [3]. To address this issue, some prevention and control strategies against corrosion have been developed [1]. These include coatings, cathodic protection, anodic protection, corrosion inhibitors, and material selection [4,5]. However, in recent years, the use of corrosion inhibitors has emerged as one of the most effective strategies for mitigating

oxidation of metallic surfaces [6]. Corrosion inhibitors are substances added to metallic materials at low concentrations to slow or prevent corrosion [7]. A wide range of inhibitors exists, encompassing both inorganic and organic compounds [6]. Among them, organic imidazole-derived molecules have demonstrated outstanding performance, maintaining high efficiency even at low concentrations and under aggressive corrosive conditions [8–10]. Their effectiveness stems from the presence of free electron pairs and π-electrons in their structure, which promote their strong adsorption onto metallic surfaces such as iron [11,12]. Furthermore, these compounds are inexpensive, low-toxicity, and easy to synthesize, making them promising candidates for sustainable corrosion protection.

Computational approaches have played a central role in elucidating the mechanisms of inhibition by imidazole derivatives, providing insight into these interactions at the atomic and molecular levels. Density Functional Theory (DFT) [13,14] is a powerful method for this, enabling precise calculations of electronic structure, including key quantum–chemical parameters that aid in predicting an inhibitor's reactivity and its interaction with a metal surface. A central concept in this field is the frontier molecular orbital (FMO) theory, which correlates a molecule's inhibiting efficiency with the energies of its highest occupied molecular orbital (HOMO) and lowest unoccupied molecular orbital (LUMO). A smaller HOMO-LUMO energy gap (ΔE) suggests higher chemical reactivity and a greater tendency toward electron transfer, resulting in improved inhibition performance [15]. The adsorption of the inhibitor molecule onto the metal surface is the primary mechanism of corrosion inhibition, which can be characterized as either physisorption (weak physical attraction) or chemisorption (strong chemical bond formation) [16]. For example, studies employing Quantum ESPRESSO have analyzed the adsorption energies of imidazole (IM) and methyl-imidazole (Me-IM) on metallic surfaces in parallel, perpendicular, and oblique orientations. These studies revealed that the parallel orientation yields the highest adsorption energy, indicating a stronger interaction [17]. In 2023, first-principles simulations combined with the tight-binding Density Functional Theory (DFTB) [18,19] were used to investigate the interaction mechanism and corrosion-inhibition performance of a new benzimidazole-based epoxy resin. The adsorption energy between the molecule and the surface was calculated considering parallel and perpendicular orientations. The results revealed the formation of covalent bonds in the parallel position, whereas no bond formation was observed in the perpendicular configuration. The DFTB method is a valuable alternative to conventional DFT for large systems, as it is 2–3 orders of magnitude faster while maintaining comparable accuracy [19].

Although DFTB has demonstrated efficacy in characterizing molecular interactions, the rational design of high-performance inhibitors is impeded by the pronounced sensitivity of adsorption energies to molecular orientation and the dynamic nature of the metal–organic interface [9,20,21]. The present study addresses these challenges by implementing an integrated multiscale computational framework that connects quantum–chemical reactivity analysis with large-scale surface modeling. This approach is exemplified through a comparative investigation of two strategically substituted triphenylimidazole derivatives: M1 and M2 (see Figure 1). Systematic mapping of the orientation-dependent adsorption landscape on the highly reactive Fe(100) surface, combined with validation of stability via time-resolved MD simulations, establishes a definitive link between subtle functional group modifications and macroscale inhibition performance. The findings identify M2 as a superior candidate for industrial steel protection and establish a robust, predictive workflow essential to the accelerated development of next-generation, sustainable, and precision-engineered corrosion inhibitors.

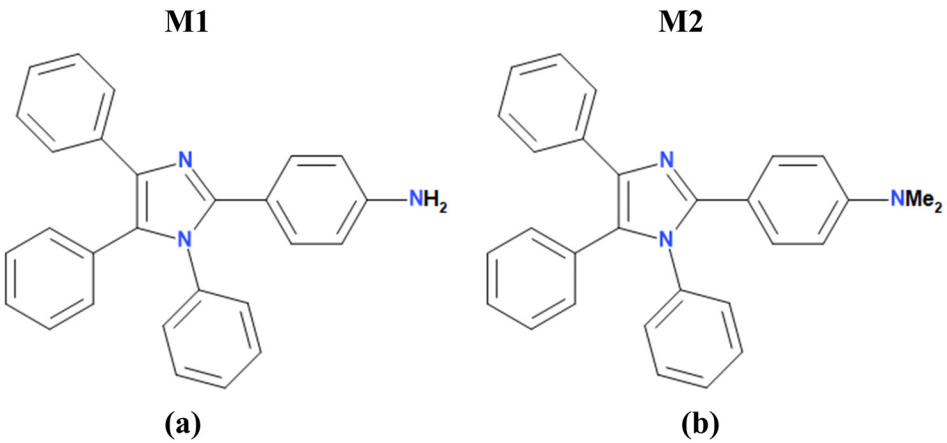

Figure 1. Chemical structures of the studied triphenylimidazole derivatives: (**a**) M1 and (**b**) M2.

2. Methods

2.1. DFT Calculations

Theoretical calculations were performed using DFT, employing the M06 functional [22] and the 6-31G(d,p) basis set [23], as implemented in the Gaussian 16 computational code [24]. The M06 functional was selected for its proven robust performance in describing systems involving organometallic chemistry and non-covalent interactions, which are crucial to the inhibitor's adsorption onto the metal surface. At the same time, the 6-31G(d,p) basis set is a split-valence double-zeta set that offers a suitable balance between accuracy and computational cost for molecules of this size. The inclusion of polarization functions (d,p) is essential, as they provide the necessary flexibility to accurately describe chemical bonds. All molecular calculations for M1 and M2 were performed in water using the Integral Equation Formalism Polarized Continuum Model (IEF-PCM) [25–27]. This solvent was specifically chosen to accurately simulate the aqueous environments in which industrial corrosion inhibition processes occur, ensuring results are physically relevant to experimental conditions [28]. Conformational analysis was performed using the rotation of the aromatic rings, the primary amine, and the dimethylamine. Molecular structures and vibrational frequencies were optimized to model a chemical structure and thus ensure that the global minimum stationary points were found. Finally, the minimum energy structure was selected.

The energy and electronic density plots of the FMOs (specifically the HOMO, LUMO, and ΔE) and the molecular electrostatic potential (MEP) were obtained at the same level of theory.

To provide a deeper understanding of the molecular reactivity, key parameters were calculated using conceptual DFT. We obtained the energies of the cation (E_{N_0-1}), anion (E_{N_0+1}), and neutral (E_{N_0}) species, also in a water solvent environment. The obtained parameters include ionization potential (I), electron affinity (A), chemical hardness (η), electrophilicity index (ω), electrodonating power (ω^-), and electroaccepting power (ω^+). The equations used for these calculations are as follows [29–33]:

$$I = (E_{N_0-1} - E_{N_0}), \quad (1)$$

$$A = (E_{N_0} - E_{N_0+1}), \quad (2)$$

$$\eta = (I - A), \quad (3)$$

$$\omega = \frac{(I + A)^2}{8(I - A)}, \quad (4)$$

$$\omega^{-} = \frac{(3I + A)^2}{16(I - A)}, \tag{5}$$

$$\omega^{+} = \frac{(I + 3A)^2}{16(I - A)}, \tag{6}$$

To further validate the accuracy of the electronic structure analysis and the resulting conceptual DFT (CDFT) descriptors, additional geometry optimization and single-point calculations were conducted at the M06/6-311G(d,p), M06-2X/6-31G(d,p), and M06-2X/6-311G(d,p) levels of theory. As indicated in the Supplementary Materials (Tables S1 and S2), transitioning to a triple-zeta basis set and employing the M06-2X functional, which improves the treatment of non-covalent interactions, resulted in minimal changes in absolute descriptor values. These findings confirm that the selected level of theory is appropriate for describing the comparative inhibition potential of these systems.

2.2. DFTB Calculations

The adsorption mechanism was initially explored using the Density Functional Tight Binding (DFTB) method, as implemented in the DFTB+ code (version 22.2) [19]. A cluster of 448 iron atoms was created with a Body-Centered Cubic (BCC) crystal structure and a Miller index of (100). The cluster was built as an ($8 \times 8 \times 7$) supercell with a 50 Å void height. This construction was performed using the Visualization for Electronic and Structural Analysis (VESTA) [34] and DFTB+ programs. For the optimization of the BCC iron surface and the molecule-iron interactions, a $1 \times 1 \times 1$ Monkhorst–Pack k-point grid was used in the Brillouin zone. The mio-1-1 [35–37] was employed to describe the organic components of the system (C, H, and N interactions), as it is a standard, widely validated parameterization for organic and biological molecules. For the iron atoms and their interactions with the inhibitor molecules, the trans3d-0-1 [38] parameter set was chosen. This set is specifically designed for modeling first-row transition metals in organometallic and biological contexts, making this combination particularly suitable for describing the hybrid metal–organic interface central to this study. The molecule–surface interactions were described using the corresponding mixed Slater–Koster files available in DFTB+.

The Fe(100) surface was selected because it is considered one of the most stable and representative iron surface orientations in theoretical studies of corrosion inhibition [39–43]. To accurately capture the most favorable adsorption configuration and identify the global energy minimum, it is essential to explore multiple adsorption sites and molecular orientations. The adsorption energy $\left(E_{adsorption}\right)$ and charge density difference $\Delta\rho(r)$ were calculated using DFTB+ with the following equations [11,44]:

$$E_{binding} = E_{total} - \left(E_{surface} + E_{molecule}\right), \tag{7}$$

$$E_{adsorption} = -E_{binding}, \tag{8}$$

$$\Delta\rho(r) = \rho_{total}(r) - [\rho_{surface}(r) + \rho_{molecule}(r)], \tag{9}$$

The charge density difference $\Delta\rho(r)$ visualization was done using Visual Molecular Dynamics (VMD) [45].

2.3. SIESTA Calculations

The lowest energy adsorption configurations identified from the DFTB calculations were subsequently used as initial structures for periodic spin polarized DFT relaxations with the SIESTA code [46,47]. Owing to the higher computational cost of the SIESTA calculations, the full Fe slab used in the DFTB+ calculations was reduced, and only the four upper Fe layers closest to the adsorbed inhibitor were retained.

During the geometry optimization, the two bottom Fe layers were kept fixed to preserve the bulk like structure of the substrate, whereas the two upper Fe layers and the inhibitor molecule were fully relaxed.

The calculations were performed using the GGA-PBE [48] exchange correlation functional and a DZP [49] numerical atomic orbital basis set. The Fe(100)-inhibitor systems were described using a 20.287 × 20.287 × 35.000 $Å^3$ simulation cell, a 1 × 1 × 1 Monkhorst–Pack k-point grid, a real space mesh cutoff of 250 Ry, a PAO energy shift of 50 meV, and a PAO split norm of 0.15. Geometry relaxations were carried out until a maximum force tolerance of 0.05 eV $Å^{-1}$ was reached. The SIESTA-relaxed structures were then used to calculate BSSE-corrected adsorption energies using the counterpoise approach, in which the energies of the frozen slab and frozen molecule in the adsorbed geometry were computed with and without ghost orbitals, using the same simulation cell and numerical parameters as the full adsorbed system.

The BSSE-corrected adsorption energy was calculated according to:

$$E_{ads}^{(BSSE-corr)} = E_{AB} - E_{A,relaxed} - E_{B,relaxed} + \Delta E_{BSSE}, \quad (10)$$

where A represents the Fe(100) slab, B the inhibitor molecule, and ΔE_{BSSE} was obtained using the counterpoise approach with frozen fragments and ghost orbitals in the adsorbed geometry.

Charge density difference analyses were additionally carried out using the relaxed structures obtained from SIESTA calculations. The corresponding results are included in the Supplementary Materials.

2.4. Molecular Dynamics Simulations with MACE

Molecular dynamics simulations were performed to evaluate the short-time stability of the adsorbed inhibitor configurations on Fe(100). The initial structures were taken from the adsorption configurations obtained from the DFTB structural search. The simulations were carried out using the MACE [50,51] machine-learning interatomic potential through the Atomic Simulation Environment (ASE) [52]. Specifically, the MACE-MH-1 foundation model was used with the OMAT_PBE head, running on a CUDA device with single-precision arithmetic.

MACE is an equivariant message-passing neural-network interatomic potential designed to provide fast and accurate energies and forces. Recent studies have shown that MACE foundation models can reproduce DFT-level trends for a broad range of molecular and condensed-phase systems, including metallic, organic, and hybrid interfaces, supporting their applicability for exploratory molecular dynamics simulations of metal–organic adsorption systems [53–55].

The MD simulations were performed in the NVT ensemble using a Langevin thermostat at 300 K. A time step of 1.0 fs was used, and each trajectory was propagated for 500 ps. The Langevin friction coefficient was set to 0.005 fs^{-1}. The bottom Fe layer was fixed during the simulations, while the remaining atoms were allowed to evolve dynamically. Initial velocities were assigned according to a Maxwell–Boltzmann distribution at 300 K. Energy and temperature data were recorded every 50 steps, and trajectory frames were written every 50 steps. The MD workflow was implemented using ASE, which provides Python version 3.9 tools for setting up, steering, and analyzing atomistic simulations.

3. Results and Discussion

A conformational analysis with various rotations was performed, as shown in Figure 2. The molecular structures of both inhibitors were optimized in the ground state using DFT at the M06/6-31G(d,p) level of theory in aqueous phase. Table 1 shows the dihedral angles

(°) of the molecular geometries and their energies. A vibrational frequency analysis was performed to confirm that the optimized structures correspond to a true minimum, with no imaginary frequencies. This confirms the preferred molecular geometry under the specific conditions of the study. The conformational analysis of M1 and M2 revealed that several conformers exhibit very similar energies, differing by less than 0.05 eV, as shown in Table 1. This indicates that they are nearly isoenergetic, suggesting a certain degree of conformational flexibility. Therefore, multiple conformations may coexist under the studied conditions. Additionally, we present structural parameters of the lowest-energy structures (bond lengths, bond angles, and dihedral angles) for inhibitors M1 and M2 in Table 2.

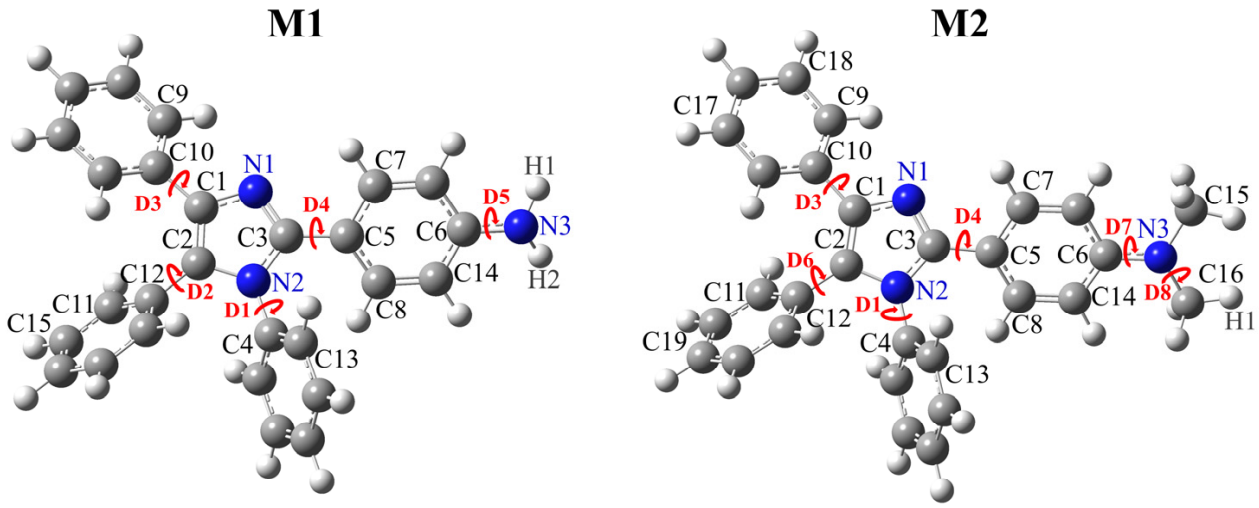

Figure 2. Optimized molecular geometries for M1 and M2, calculated at the M06/6-31G(d,p) level of calculation in aqueous phase. Nitrogen atoms are shown in blue, carbon atoms in dark gray, and hydrogen atoms in light gray.

Table 1. Conformational analysis of M1 and M2: Angles and Energy of the optimized structures.

M1				
Conformer	**Dihedral Definition**	**Angle Initial (°)**	**Angle End (°)**	**Energy (eV)**
D1	C3-N2-C4-C13	−15.63	65.40	−32,788.260
D2	C11-C12-C2-C1	145.30	55.56	−32,788.260
D3	C9-C10-C1-N1	−62.57	25.27	−32,788.260
D4	N1-C3-C5-C7	−61.15	−24.82	−32,788.208
D5	C14-C6-N3-H2	−20.91	−23.77	−32,788.259
M2				
D1	C3-N2-C4-C13	−42.29	64.74	−34,925.610
D3	C9-C10-C1-N1	−62.62	25.15	−34,925.610
D4	N1-C3-C5-C7	−54.32	−23.90	−34,925.565
D6	C11-C12-C2-N2	147.03	−122.18	−34,925.610
D7	H1-C16-N3-C15	90.82	4.59	−34,925.610
D8	C14-C6-N3-C16	10.39	10.43	−34,925.610

Table 2. Comparison of structural parameters, including bond lengths, bond angles, and dihedral angles, for the optimized M1 and M2 molecules.

	M1	M2
Parameters	**Angles (°)**	**Angles (°)**
C6−N3−H1	116.07	-
H1−N3−H2	112.62	-
C6−N3−C15	-	119.80
C15−N3−C16	-	119.64
C9−C10−C1−N1	25.26	25.15
C11−C12−C2−C1	55.52	54.36
C3−N2−C4−C13	65.36	64.70
N1−C3−C5−C7	28.79	27.82
C14−C6−N3−H2	23.19	-
C14−C6−N3−C16	-	4.57
H1−C16−N3−C15	-	10.39

The minimum energy structures of both inhibitors are largely similar, but there is a significant structural difference in the environment surrounding the N3 atom, due to their substituents; M1 has an amine group, and M2 has a dimethylamine group. The amine group in M1 exhibits a pyramidal geometry with the C6 fragment, as observed in (C6-N3-H1 = 116.07° and H1-N3-H2 = 112.62°). It also shows appreciable torsion at C6 (C14-C6-N3-H2 = 23.19°), which reduces conjugation. The dimethylamine group in M2 exhibits near planarity, with angles close to 120° (C6-N3-C15 = 119.80° and C15-N3-C16 = 119.64°) and torsions close to 0–10° (C14-C6-N3-C16 = 4.57° and H1-C16-N3-C15 = 10.39°). In other words, M2 exhibits higher planarity and conjugation at the N3 atom than M1. The increased planarity of M2 allows greater orbital overlap with the metal surface, favoring the formation of a more compact and stable protective film. Consequently, M2 is expected to exhibit a slightly more favorable adsorption behavior than M1 [56].

The complete XYZ coordinates of M1 and M2 are provided in the Supplementary Materials.

Analysis of the electron density distributions of the HOMO, LUMO, and FMOs of the studied compounds allows identification of electron-donor and electron-acceptor regions, corresponding to nucleophilic and electrophilic sites, respectively. This information is crucial for determining the viability of the inhibition process [20]. Figure 3 depicts the FMOs of the two corrosion inhibitors, along with their energy levels and respective ΔE.

As observed in both compounds, the electron density of the HOMO is distributed throughout the inhibitor, with a predominant concentration near the nitrogen heteroatoms and the aromatic rings. This suggests that both molecules can donate electrons to the metal surface. In contrast, the LUMO electron density is delocalized over both molecules, indicating a capacity to accept electrons from the metallic surface [57]. The exception is the methyl groups, which do not contribute to the electron-accepting regions. The HOMO and LUMO energy levels and their ΔE are also shown in Figure 3. The inhibitor M2 has a higher HOMO energy (−5.275 eV) than M1 (−5.447 eV). Higher HOMO energy indicates a greater tendency to donate electrons, while a low LUMO energy indicates a stronger capacity to accept electrons. The calculated LUMO energies for M1 (−0.743 eV) and M2 (−0.736 eV) are highly similar, differing by only 0.007 eV. This similarity demonstrates that the structural modification from a primary amine to a dimethylamine substituent exerts minimal influence on electron-accepting capacity. The stability of the LUMO energy level is attributed to its localization over the shared π-conjugated framework, specifically the triphenylimidazole core, which is largely unaffected by substituents at the C2 position. These findings indicate that, although electron-donating properties are significantly influenced by functionalization, electron-accepting behavior is primarily governed by the core scaffold.

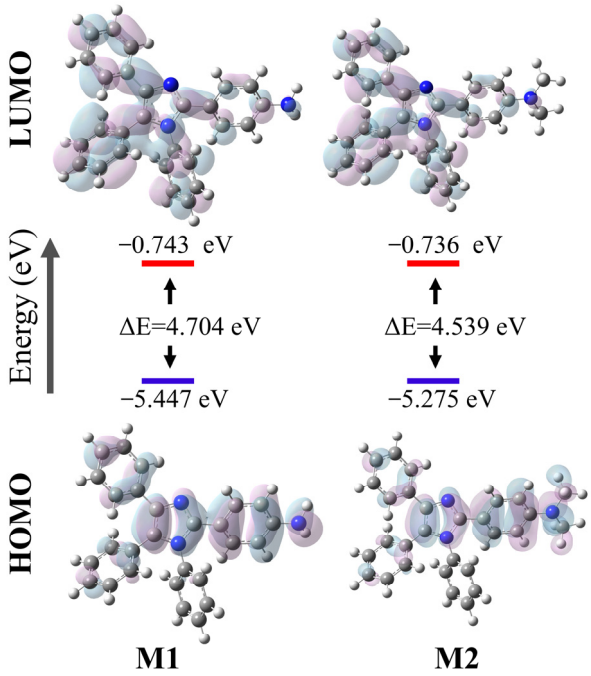

Figure 3. Spatial distribution of FMO (HOMO and LUMO), energy levels, and calculated ΔE for M1 and M2.

This suggests a stronger interaction between the heterocycle's π electrons and the vacant *d* orbitals of the iron surface atoms [58]. The ΔE is another important parameter for inhibitor efficiency; as lower values correspond to greater reactivity and, consequently, enhanced inhibition performance [59,60]. In this study, M2 exhibits a lower ΔE of 4.539 eV than M1, 4.704 eV, which is consistent with the electronic influence of the dimethylamine substituent [9]. This smaller ΔE indicates that M2 is more reactive and serves as a superior corrosion inhibitor [61].

MEP was used to identify reactive sites for electrophilic and nucleophilic attack by mapping the electron density distribution within the molecules [62], as shown in Figure 4. Regions of negative potential (red) correspond to electron-rich areas, while regions of positive potential (blue) indicate electron-deficient sites and electron acceptors [63]. As shown in Figure 4, electron-rich regions are primarily located around the nitrogen atoms of the imidazole in both molecules. In contrast, electron-deficient regions are mainly associated with the hydrogen atoms. A notable difference between the two systems is that M2 exhibits a more intense and broader negative potential, particularly around the $-NMe_2$ group, suggesting a higher local electron density around the substituent region, which may favor interactions with the metal surface.

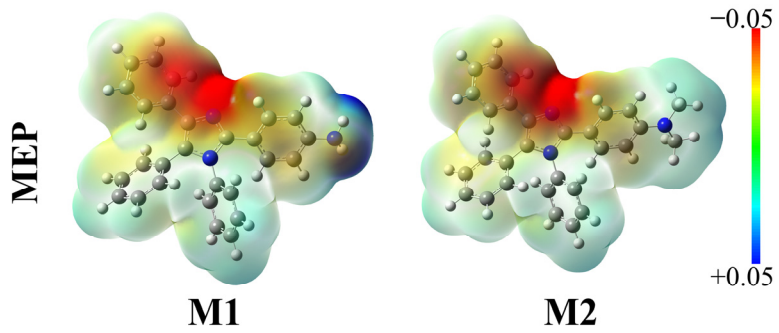

Figure 4. MEP of M1 and M2 inhibitor; the color code thresholds are red −0.05 and blue +0.05.

The chemical reactivity parameters are presented in Table 3. Chemical hardness (η), electrophilicity index (ω), electrodonating power (ω^-), and electroaccepting power (ω^+) are key parameters for understanding the interaction of the inhibitors with the metal surface [64].

Table 3. Global reactivity descriptors and quantum chemical parameters for M1 and M2 were calculated using Conceptual Density Functional Theory (CDFT) at the M06/6-31G(d,p) level of theory, employing water as the solvent medium to simulate a realistic aqueous environment.

Parameters (eV)	M1	M2
η	4.124	3.969
ω	1.175	1.155
ω^-	4.164	4.070
ω^+	1.051	1.046

Chemical hardness represents the resistance that chemical systems present to intramolecular charge transfer [65]. Low chemical hardness values indicate high chemical reactivity, attributed to strong interactions between the molecule and the metal surface, thereby increasing its efficiency as a corrosion inhibitor. Inhibitor M2 has a lower hardness 3.969 eV and exhibits a dimethylamine group on a benzene ring, in contrast to inhibitor M1, which has a value of 4.124 eV and contains an amine as a substituent. The electronic influence of the substituent contributes to higher molecular reactivity [20].

The electrophilicity index (ω) of a molecule is an important indicator of its efficiency as a corrosion inhibitor [66]. The electrophilicity index provides information about the energetic stabilization that occurs when a molecule acquires an additional charge from its environment. The high value of this index suggests greater stabilization capacity of the molecule [67]. M1 shows a slightly higher electrophilicity index than M2.

Electrodonating power (ω^-) measures a molecule's tendency to donate charge. The lower the electrodonating power, the greater the molecule's ability to donate electrons [33]. Inhibitor M2 exhibits a slightly lower electrodonating power value 4.070 eV than M1, consistent with its enhanced donor character. The electroaccepting power (ω^+) measures a molecule's tendency to accept a charge. A higher value of this parameter denotes a greater capacity of the molecule to accept electrons [33]. Inhibitors M1 and M2 have similar electroaccepting power (1.051 eV and 1.046 eV, respectively) despite their different substituents.

The minimal difference in the corresponding electroaccepting powers (ω^+) between M1 and M2 suggests that the structural modification from a primary amine to a dimethylamine substituent has a negligible impact on the molecules' ability to accept electrons. This stability indicates that the core triphenylimidazole scaffold intrinsically determines the electron-accepting behavior. In general, while electron-donating groups (EDGs), such as those studied here, tend to increase molecular electron density and may slightly raise the LUMO energy, the introduction of electron-withdrawing substituents would be required to significantly lower the LUMO energy and enhance the electron-accepting capacity (ω^+).

The studied molecules exhibit both electron-donating and electron-accepting interactions with the metal surface, mainly associated with the nitrogen atoms and aromatic rings. Overall, the electronic descriptors suggest slightly more favorable adsorption-related properties for M2.

Calculations using the DFTB method have proven highly efficient for simulating interactions between inhibitor molecules and the metal surface [18]. Typically, studies of adsorption energy have been conducted by placing the molecules perpendicular or parallel to the metal surface [5,68]. The aim was to identify the minimum-energy adsorption configuration. Figure 5 shows different positions in which the molecule was placed on the

metal surface (every 45°). The total energy for inhibitors M1 and M2 in these positions is presented in Table 4. The relative energies (ΔE) were referenced to the lowest-energy configuration for each molecule individually. The relative orientation angle was defined with respect to the surface plane using selected reference atoms; therefore, it should be considered an approximate descriptor, given the molecule's non-planar nature.

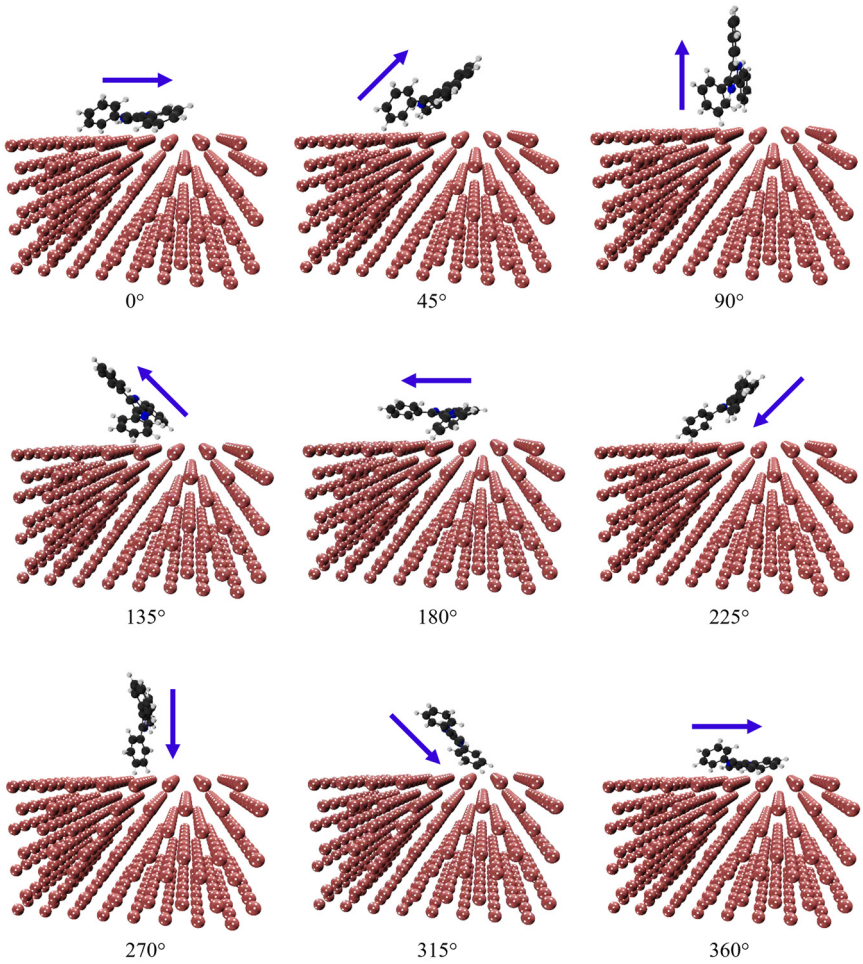

Figure 5. Schematic representation of the molecular orientation mapping (rotated at 45° intervals) relative to the Fe(100) surface for adsorption site evaluation, performed using the DFTB method with the mio-1-1 and trans3d-0-1 parameter sets, as implemented in DFTB+.

Table 4. Total system energies in eV calculated as a function of molecular orientation angle on the Fe(100) surface.

	M1		M2	
Location	**Energy**	**ΔE**	**Energy**	**ΔE**
0°	−20,296.148	1.269	−20,430.806	0.153
45°	−20,295.811	1.605	−20,430.959	0.000
90°	−20,296.116	1.301	−20,429.789	1.170
135°	−20,295.214	2.203	−20,430.882	0.078
180°	−20,296.456	0.961	−20,430.352	0.607
225°	−20,296.559	0.858	−20,430.746	0.213
270°	−20,292.435	4.982	−20,426.408	4.551
315°	−20,295.433	1.984	−20,429.773	1.187
360°	−20,297.417	0.000	−20,429.477	1.482

According to the results, the minimum-energy state for M1 occurs when the molecule is parallel to the surface (360°), whereas for M2 it occurs at 45°. Full geometry optimizations on the surface allow the system to relax and inherently account for conformational changes upon adsorption. Both inhibitors have proven to be good candidates for corrosion inhibition, as they adsorb onto the iron surface after optimization, thereby enhancing their interaction with the surface.

The adsorption energy (E_{ads}), a critical parameter for distinguishing between physisorption and chemisorption, was calculated to evaluate the inhibitor-surface interaction. Weak van der Waals interactions characterize physisorption forces, with energies typically $\geq$0.3 eV [69]. In contrast, chemisorption involves the formation of strong chemical bonds, with energies typically 1–3 eV for single organic molecules on metal surfaces. In this study, the calculated adsorption energies for M1 and M2 were −12.673 eV and −12.912 eV, respectively.

Although these values indicate a strong interaction between the inhibitors and the Fe(100) surface, their unusually large magnitude suggests that the adsorption strength may be overestimated at the DFTB level. Therefore, DFTB calculations were primarily used to identify favorable adsorption configurations, while the final quantitative adsorption energies were obtained from subsequent SIESTA calculations.

Starting from the lowest energy adsorption configurations obtained with DFTB, additional spin polarized DFT relaxations were carried out using SIESTA. After this refinement, the overall adsorption motifs were preserved, although some local variations in the molecule–surface geometry were observed (see Supplementary Material). This indicates that the DFTB calculations provided suitable initial adsorption configurations, while the SIESTA calculations offered a more reliable quantitative description of the adsorption energetics. The uncorrected SIESTA adsorption energies were −7.371 eV for M1 and −7.533 eV for M2. After applying the BSSE corrections of +3.525 eV and +3.677 eV, respectively, the final BSSE-corrected adsorption energies were −3.846 eV for M1 and −3.856 eV for M2. These corrected values are considerably smaller in magnitude than the original DFTB estimates, providing a more conservative quantitative description of the molecule–surface interaction.

Table 5 compares the adsorption energies obtained using DFTB and SIESTA calculations. The considerably higher adsorption energies predicted by DFTB may be associated with the approximate nature of the semi-empirical parameterization and the method's limitations in quantitatively describing charge transfer and metal–organic interactions on transition metal surfaces. Therefore, DFTB was primarily employed to identify favorable adsorption configurations, while SIESTA calculations were used for the quantitative evaluation of adsorption energies.

Table 5. Comparative adsorption energies obtained from DFTB and SIESTA calculations for M1 and M2 adsorbed on Fe(100). All values are given in eV.

Method	M1 (eV)	M2 (eV)
DFTB	−12.673	−12.912
SIESTA (uncorrected)	−7.371	−7.533
SIESTA+BSSE	−3.846	−3.856

The slightly more negative adsorption energy obtained for M2 indicates a slightly more favorable interaction with the Fe(100) surface compared with M1. Although the difference between BSSE-corrected adsorption energies is small, this trend is consistent with the electronic-structure analysis discussed above, where M2 exhibits a higher HOMO energy, a smaller HOMO–LUMO gap. Thus, the refined SIESTA results suggest a slightly better

interaction of M2 with the Fe(100) surface, while avoiding the overestimation associated with the direct DFTB adsorption energies.

A reasonable agreement was observed between the adsorption geometries obtained using DFTB+ and SIESTA, with the overall molecule–surface adsorption configurations remaining preserved after DFT refinement (see Supplementary Material). Although some local variations were observed in selected interatomic distances, no major structural rearrangements occurred. These results support the use of the DFTB+ geometries for the structural characterization and charge density difference calculations discussed below, while the SIESTA calculations were primarily employed for the quantitative evaluation of adsorption energies.

In Figure 6, the bond distances of inhibitors M1 and M2 to the atoms closest to the iron surface are shown. Selected principal interatomic distances are additionally summarized in Supplementary Table S5 for clarity. The C–Fe distance is 4.14 Å, obtained as the algebraic sum of the van der Waals radii of carbon (1.70 Å [70]) and iron (2.44 Å [71]). The shorter distances observed for M1 and M2 are consistent with significant molecule–surface interactions, allowing effective orbital overlap between the π electrons of the aromatic ring and the *d* orbitals of the iron atoms [39].

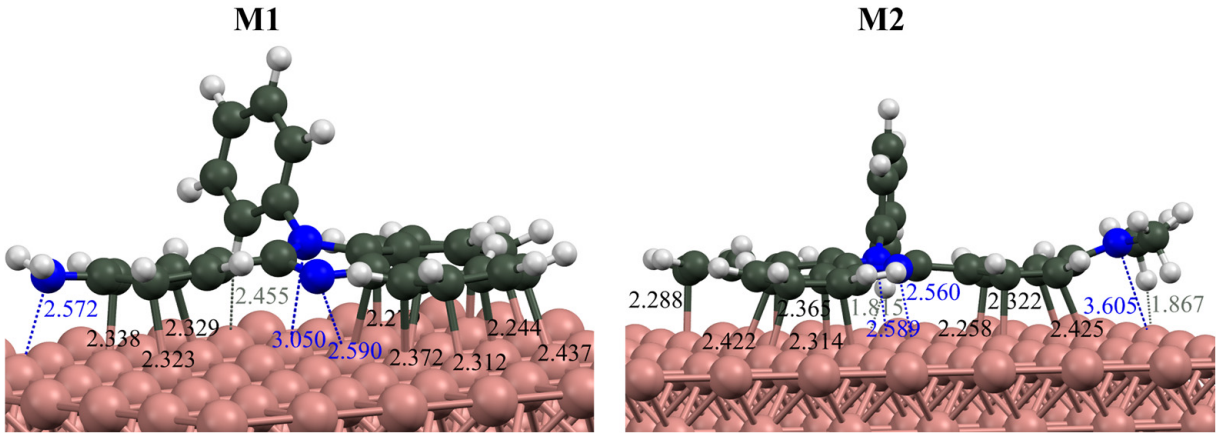

Figure 6. Optimized adsorption configurations and principal interatomic distances (in Å) between M1 and M2 inhibitors and Fe(100) surface atoms, calculated using the DFTB method with the mio-1-1 and trans3d-0-1 parameter sets, as implemented in DFTB+. Selected numerical values are summarized in Supplementary Table S5.

The van der Waals radius of the hydrogen atom is 1.20 Å [57]; therefore, the expected H···Fe interaction distance is 3.64 Å. However, the H···Fe distance obtained for M1 is 2.455 Å, and in M2 is 1.867 Å and 1.815 Å, which suggests a significant C–H···Fe interaction. The sum of the van der Waals radius of nitrogen (1.55 Å [57]) and Fe is 3.99 Å; the values obtained for inhibitors M1 and M2 are less than 3.050 Å and 3.605 Å, respectively, which is consistent with a relevant contribution of chemisorptive interactions [39].

Most atoms of the inhibitors participate in interactions with the metal surface. The only atoms that do not participate in the interaction are those of the benzene ring, which becomes oriented perpendicular to the surface after optimization. These results indicate that both M1 and M2 interact favorably with the Fe(100) surface, with adsorption characteristics consistent with significant chemisorptive contributions.

To validate the claim of chemisorption, a charge density difference analysis was performed, as shown in Figure 7. The regions of electron density enrichment are colored purple, whereas the regions of electron density loss are colored light blue. These charge redistribution regions are mainly located between the inhibitors M1 and M2 and the iron surface. The electron transfer occurs between the π electrons of the heterocyclic com-

pound and the vacant "*d*" orbitals of the metal surface atoms. These results are consistent with charge redistribution at the molecule–surface interface and support the presence of significant electronic interactions between the inhibitors and the Fe(100) surface [17].

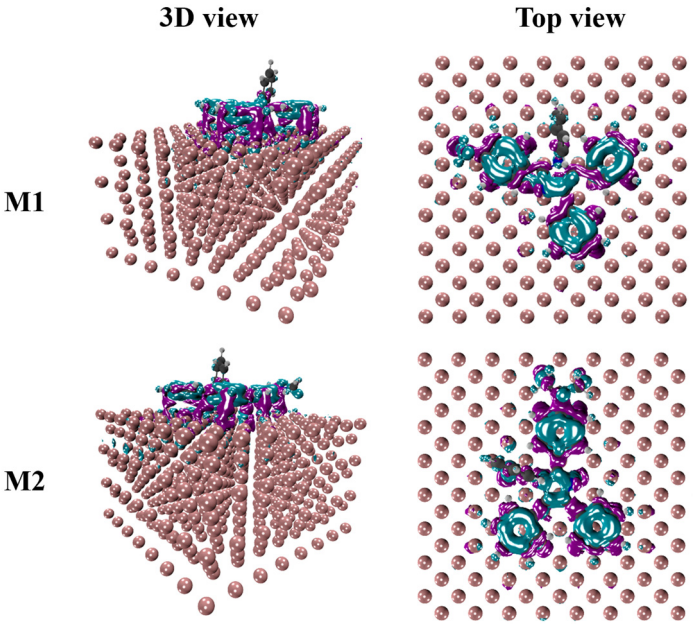

Figure 7. Charge density difference maps ($\Delta\varrho$(r)) for M1 and M2 adsorbed on the Fe(100) surface, obtained using the DFTB method with the mio-1-1 and trans3d-0-1 parameter sets. Purple regions indicate electron density enrichment, while light blue regions indicate electron density depletion.

Molecular dynamics simulations were performed to investigate the interactions between the inhibitors and the Fe(100) surface. The stability of the adsorption configurations was evaluated as a function of time and temperature. Figure 8 presents the evolution of the total potential energy for each inhibitor during the 500 ps simulations, showing relatively stable thermal and energetic behavior throughout the simulation.

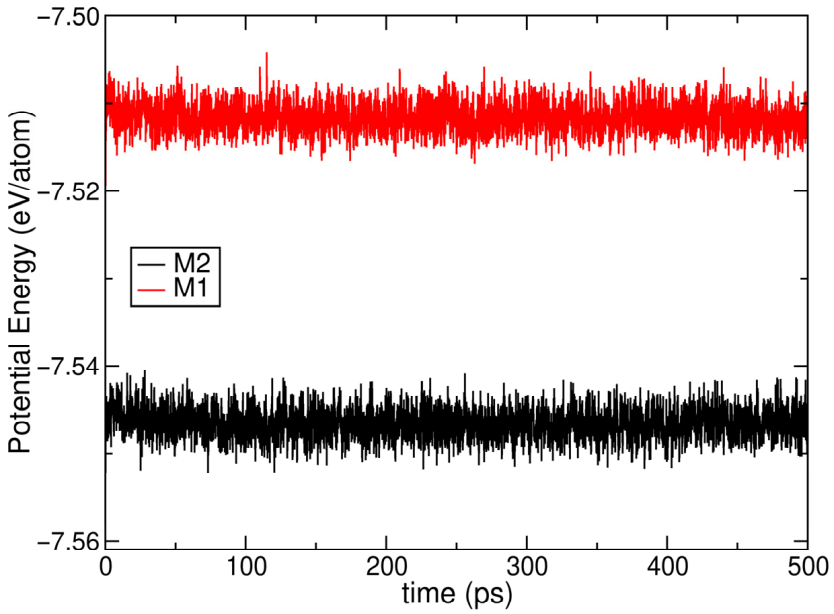

Figure 8. Temporal evolution of potential energy during the MD simulations of M1 and M2 on the Fe(100) surface at 300 K.

Additionally, Figure 9 shows the time evolution of representative N−Fe and C−Fe interatomic distances during the MD simulations. The absence of large-distance fluctuations or progressive separation from the surface further supports the persistence of the adsorbed configurations over the simulated timescale. These results suggest that the systems reached thermal and structural equilibrium during the simulated timescale.

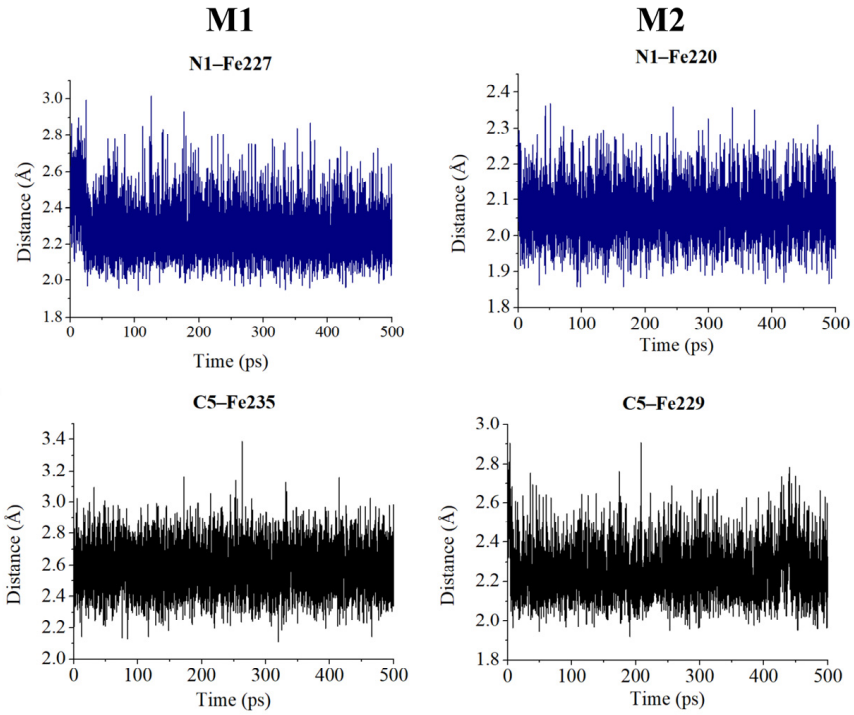

Figure 9. Time evolution of representative N−Fe and C−Fe interatomic distances during the MD simulations of M1 and M2 adsorbed on the Fe(100) surface.

Both molecules remained adsorbed during the simulations, indicating stable adsorption behavior over the short simulation timescale investigated in this work. In the case of M2, a slight reorientation of one aromatic ring interacting with the surface was observed at the beginning of the simulation; however, the molecule maintained a stable adsorption configuration afterward (see Supplementary Material). Nevertheless, the present MD simulations capture only short-term dynamical behavior and do not allow conclusions about long-term adsorption stability or macroscopic corrosion-inhibition performance.

4. Conclusions

The analysis of FMO (HOMO and LUMO), ΔE, MEP, and chemical reactivity parameters consistently indicates that both M1 and M2 molecules are promising corrosion inhibitors. The findings reveal that M2, which is substituted with a dimethylamine group, exhibits slightly better inhibition performance than M1, which contains a primary amine. This enhanced performance is attributed to the dimethylamine group ($-NMe_2$), which acts as a more potent electron donor due to the combined inductive and resonance effects of its methyl groups. The lower ΔE of M2 (4.539 eV) compared to M1 (4.704 eV) further confirms its higher chemical reactivity and superior electron-transfer capability, suggesting somewhat improved inhibition performance.

Adsorption energy calculations, along with interatomic distance analysis and charge density difference maps, indicate significant interactions between the inhibitor molecules and the Fe(100) surface. The corrected adsorption energies (−3.846 eV for M1 and −3.856 eV for M2), combined with the short molecule–surface distances and the observed charge

redistribution, suggest that the adsorption mechanism involves a significant chemisorptive contribution associated with electron donor–acceptor interactions between the inhibitors and the metal surface. Although some local geometric differences were observed between the DFTB+ and SIESTA-optimized structures, the overall adsorption configurations remained unchanged after DFT refinement.

Furthermore, molecular dynamics simulations showed that both inhibitors, M1 and M2, remained adsorbed on the iron surface at 300 K throughout the simulation, maintaining stable molecule–surface interactions over the simulated timescale. The stabilization of the potential energy profiles, together with the relatively stable N−Fe and C−Fe interatomic distances observed during the simulations, supports the persistence of the adsorbed configurations under the studied conditions. However, the present molecular dynamics simulations only capture short-term dynamic behavior and therefore do not allow conclusions about long-term adsorption stability or macroscopic corrosion inhibition performance.

This study suggests that M2 may exhibit improved inhibition performance compared with M1, mainly due to the electronic and structural effects associated with the dimethylamine substituent. The calculated electronic descriptors, adsorption behavior, and molecular dynamics simulations consistently indicate somewhat stronger molecule–surface interactions for M2. These findings provide useful theoretical insight into the design of corrosion inhibitors for iron surfaces and may contribute to the future development of related anti-corrosion materials.

Supplementary Materials: The following supporting information can be downloaded at: https://www.mdpi.com/article/10.3390/org7020021/s1, Figure S1: Structural comparison of M1 with different levels of theory (M06/6-31G(d,p), M06/6-311G(d,p), M06-2X/6-31G(d,p) and M06-2X/6-311G(d,p)); Figure S2: Structural comparison of M2 with different levels of theory (M06/6-31G(d,p), M06/6-311G(d,p), M06-2X/6-31G(d,p) and M06-2X/6-311G(d,p)); Table S1: Global reactivity descriptors of M1 obtained using different functionals and basis sets; Table S2: Global reactivity descriptors of M1 obtained using different functionals and basis sets; Table S3: XYZ coordinates of the M1 inhibitor optimized with M06/6-31G(d,p) using water as solvent; Table S4: XYZ coordinates of the M2 inhibitor optimized with M06/6-31G(d,p) using water as solvent; Figure S3: Optimized adsorption configurations and principal interatomic distances (in Å) between M1 and M2 inhibitors and Fe(100) surface atoms, calculated using SIESTA; Table S5: Comparison of selected atom–surface interaction distances obtained from DFTB and DFT calculations for M1 and M2 adsorbed on Fe(100).

Author Contributions: Conceptualization, A.N.-M., J.P.P.-B., R.S.-R., T.D.-M., S.S.-A., N.A.S.-B., D.G.-M. and J.B.-L.; Formal Analysis, A.N.-M., J.P.P.-B., R.S.-R., T.D.-M., S.S.-A., N.A.S.-B., D.G.-M. and J.B.-L.; Investigation, A.N.-M., J.P.P.-B., D.G.-M. and J.B.-L.; Methodology, A.N.-M., J.P.P.-B., R.S.-R., T.D.-M., S.S.-A., N.A.S.-B., D.G.-M. and J.B.-L.; Supervision, J.P.P.-B. and J.B.-L.; Writing—Original Draft, A.N.-M., J.P.P.-B., D.G.-M. and J.B.-L.; Writing—Review and Editing, R.S.-R., T.D.-M., S.S.-A., N.A.S.-B., D.G.-M. and J.B.-L. All authors have read and agreed to the published version of the manuscript.

Funding: This research received no funding.

Data Availability Statement: The data supporting the findings of this study are available from the corresponding author upon reasonable request. Structural comparisons obtained using different levels of theory, global reactivity descriptors calculated with different functionals and basis sets, optimized XYZ coordinates of the inhibitors, and comparisons of selected atom–surface interaction distances obtained using different computational methods are included in the Supplementary Material.

Acknowledgments: The authors express their sincere gratitude to Rodrigo Domínguez of CIMAV for his valuable technical assistance. We also thank Luis Ángel Sánchez Castillo of UAS for his advice and support in preparing the figures for the manuscript. Andrea Navarrete-Mosquera acknowledges the support of a fellowship grant Nº 4031868 from SECIHTI (México). Jesús Baldenebro-López, Rody

Soto-Rojo, Tomás Delgado-Montiel, Samuel Soto-Acosta, and Manuel Luque-Román are affiliated researchers at the Universidad Autónoma de Sinaloa; Juan Pedro Palomares-Báez and Nora Aydee Sánchez-Bojorge are affiliated researchers at the Universidad Autónoma de Chihuahua; Daniel Glossman-Mitnik is an affiliated researcher at the Centro de Investigación en Materiales Avanzados (CIMAV) and a member of the Sistema Nacional de Investigadoras e Investigadores (SNII) of the Secretaría de Ciencia, Humanidades, Tecnología e Innovación (SECIHTI), México. The authors gratefully acknowledge the computing time granted by LANCAD and SECIHTI on the supercomputer Miztli at DGTIC UNAM.

Conflicts of Interest: The authors declare no conflicts of interest.

Abbreviations

The following abbreviations are used in this manuscript:

M1	4-(1,4,5-triphenylimidazol-2-yl)-aniline
M2	*N*,*N*-dimethyl-4-(1,4,5-triphenylimidazol-2-yl)-aniline
IM	Imidazole
Me-IM	Methyl-imidazole
DFT	Density Functional Theory
DFTB+	Density-Functional Tight-Binding
MD	Molecular Dynamics
HOMO	Highest occupied molecular orbital
LUMO	Lowest unoccupied molecular orbital
ΔE	HOMO-LUMO energy gap
FMO	Frontier molecular orbital
MEP	Molecular electrostatic potential
IEF-PCM	Integral Equation Formalism Polarized Continuum Model
BCC	Body-Centered Cubic

References

1. Askeland, D.; Wright, W. *Ciencia e Ingeniería de Materiales*, 7th ed.; CENGAGE Learning: Ciudad de México, Mexico, 2016.
2. Ouakki, M.; Galai, M.; Rbaa, M.; Abousalem, A.; Lakhrissi, B.; Touhami, M.; Cherkaoui, M. Electrochemical, Thermodynamic and Theoretical Studies of Some Imidazole Derivatives Compounds as Acid Corrosion Inhibitors for Mild Steel. *J. Mol. Liq.* **2020**, *319*, 114063. [CrossRef]
3. Kumar, P.; Holmberg, K.; Soni, I.; Islam, N.; Kumar, M.; Shandilya, P.; Sillanpää, M.; Chauhan, V. Advancements in Ionic Liquid-Based Corrosion Inhibitors for Sustainable Protection Strategies: From Experimental to Computational Insights. *Adv. Colloid Interface Sci.* **2024**, *333*, 103303. [CrossRef]
4. Praveen, B.M.; Chakravarthy, A.S.J.; Prasanna, B.M.; Shabanbanu; Devendra, B.K.; Pavithra, M.K.; Fasiulla. Experimental and Theoretical Investigation of Cyclohexanone Derivative (CHD) as a Corrosion Inhibitor for Mild Steel in 1 M HCl. *Sci. Rep.* **2025**, *15*, 720. [CrossRef]
5. Damej, M.; Molhi, A.; Lgaz, H.; Hsissou, R.; Aslam, J.; Benmessaoud, M.; Rezki, N.; Lee, H.; Lee, D. Performance and Interaction Mechanism of a New Highly Efficient Benzimidazole-Based Epoxy Resin for Corrosion Inhibition of Carbon Steel in HCl: A Study Based on Experimental and First-Principles DFTB Simulations. *J. Mol. Struct.* **2023**, *1273*, 134232. [CrossRef]
6. Desai, P.; Pawar, C.; Avhad, M.; More, A. Corrosion Inhibitors for Carbon Steel: A Review. *Vietnam J. Chem.* **2023**, *61*, 15–42. [CrossRef]
7. Umoren, S.; Solomon, M. Effect of Halide Ions on the Corrosion Inhibition Efficiency of Different Organic Species—A Review. *J. Ind. Eng. Chem.* **2015**, *21*, 81–100. [CrossRef]
8. Wen, J.; Zhang, X.; Liu, Y.; Shang, B.; He, J.; Li, L. Exploration of Imidazol-4-Methylimine Thiourea as Effective Corrosion Inhibitor for Mild Steel in Hydrochloric Medium: Experimental and Theoretical Studies. *Colloids Surf. A Physicochem. Eng. Asp.* **2023**, *674*, 131895. [CrossRef]
9. Belkheiri, A.; Dahmani, K.; Aribou, Z.; Kharbouch, O.; Nordine, E.; El Moutaouakil Ala Allah, A.; Galai, M.; Touhami, M.; Al-Sadoon, M.; Al-Maswari, B.; et al. In-Depth Study of a Newly Synthesized Imidazole Derivative as an Eco-Friendly Corrosion Inhibitor for Mild Steel in 1 M HCl: Theoretical, Electrochemical, and Surface Analysis Perspectives. *Int. J. Electrochem. Sci.* **2024**, *19*, 100768. [CrossRef]

10. Dahmani, K.; Ala, M.; Aribou, Z.; Kharbouch, O.; Galai, M.; Almeer, R.; Touhami, M.; Ramli, Y.; Cherkaoui, M.; Chaouiki, A.; et al. Imidazole Derivative for Corrosion Protection: A Comprehensive Theoretical and Experimental Study on Mild Steel in Acidic Environments. *Colloids Surf. A Physicochem. Eng. Asp.* **2025**, *704*, 135376. [CrossRef]
11. Ouakki, M.; Galai, M.; Cherkaoui, M. Imidazole Derivatives as Efficient and Potential Class of Corrosion Inhibitors for Metals and Alloys in Aqueous Electrolytes: A Review. *J. Mol. Liq.* **2022**, *345*, 117815. [CrossRef]
12. Di, Y.; Lu, Y.; Li, X.; Chen, Z.; Yang, W. Fluorocarbon Chain-Based Imidazoline Derivatives as Highly Efficient Corrosion Inhibitors at Elevated Temperatures. *J. Mol. Struct.* **2023**, *1282*, 135266. [CrossRef]
13. Hohenberg, P.; Kohn, W. Inhomogeneous Electron Gas. *Phys. Rev.* **1964**, *136*, 864–871. [CrossRef]
14. Kohn, W.; Sham, L. Self-Consistent Equations Including Exchange and Correlation Effects. *Phys. Rev.* **1965**, *140*, 1133–1138. [CrossRef]
15. Berdimurodov, E.; Kholikov, A.; Akbarov, K.; Xu, G.; Abdullah, A.; Hosseini, M. New Anti-Corrosion Inhibitor (3ar,6ar)-3a,6a-Di-p-Tolyltetrahydroimidazo[4,5-d]Imidazole-2,5(1 h,3h)-Dithione for Carbon Steel in 1 M HCl Medium: Gravimetric, Electrochemical, Surface and Quantum Chemical Analyses. *Arab. J. Chem.* **2020**, *13*, 7504–7523. [CrossRef]
16. Prasad, D.; Dagdag, O.; Safi, Z.; Wazzan, N.; Guo, L. Cinnamoum Tamala Leaves Extract Highly Efficient Corrosion Bio-Inhibitor for Low Carbon Steel: Applying Computational and Experimental Studies. *J. Mol. Liq.* **2022**, *347*, 118218. [CrossRef]
17. Bousba, S.; Allal, H.; Damous, M.; Maza, S. Computational DFT Analysis and Molecular Modeling on Imidazole Derivatives Used as Corrosion Inhibitors for Aluminum in Acidic Media. *Comput. Theor. Chem.* **2023**, *1225*, 114168. [CrossRef]
18. Hourahine, B.; Aradi, B.; Blum, V.; Bonafé, F.; Buccheri, A.; Camacho, C.; Cevallos, C.; Deshaye, M.; Dumitric, T.; Dominguez, A.; et al. DFTB+, a Software Package for Efficient Approximate Density Functional Theory Based Atomistic Simulations. *J. Chem. Phys.* **2020**, *152*, 124101. [CrossRef]
19. Hourahine, B.; Berdakin, M.; Bich, J.A.; Bonafé, F.P.; Camacho, C.; Cui, Q.; Deshaye, M.Y.; Díaz Mirón, G.; Ehlert, S.; Elstner, M.; et al. Recent Developments in DFTB+, a Software Package for Efficient Atomistic Quantum Mechanical Simulations. *J. Phys. Chem. A* **2025**, *129*, 5373–5390. [CrossRef]
20. Toghan, A.; Khairy, M.; Huang, M.; Farag, A. Electrochemical, Chemical and Theoretical Exploration of the Corrosion Inhibition of Carbon Steel with New Imidazole-Carboxamide Derivatives in an Acidic Environment. *Int. J. Electrochem. Sci.* **2023**, *18*, 100072. [CrossRef]
21. Zhang, L.; He, Y.; Zhou, Y.; Yang, R.; Yang, Q.; Qing, D.; Niu, Q. A Novel Imidazoline Derivative as Corrosion Inhibitor for P110 Carbon Steel in Hydrochloric Acid Environment. *Petroleum* **2015**, *1*, 237–243. [CrossRef]
22. Zhao, Y.; Truhlar, D. The M06 Suite of Density Functionals for Main Group Thermochemistry, Thermochemical Kinetics, Noncovalent Interactions, Excited States, and Transition Elements: Two New Functionals and Systematic Testing of Four M06-Class Functionals and 12 Other Function. *Theor. Chem. Acc.* **2008**, *120*, 215–241. [CrossRef]
23. Ditchfield, R.; Hehre, W.; Pople, J. Self-Consistent Molecular-Orbital Methods. IX. An Extended Gaussian-Type Basis for Molecular-Orbital Studies of Organic Molecules. *J. Chem. Phys.* **1971**, *54*, 724. [CrossRef]
24. Frisch, M.J.; Trucks, G.W.; Schlegel, H.B.; Scuseria, G.E.; Robb, M.A.; Cheeseman, J.R.; Scalmani, G.; Barone, V.; Petersson, G.A.; Nakatsuji, H.; et al. *Gaussian 16, Revision C.01*; Gaussian Inc.: Wallingford, CT, USA, 2016.
25. Miertuš, S.; Scrocco, E.; Tomasi, J. Electrostatic Interaction of a Solute with a Continuum. A Direct Utilizaion of AB Initio Molecular Potentials for the Prevision of Solvent Effects. *Chem. Phys.* **1981**, *55*, 117–129. [CrossRef]
26. Miertuš, S.; Tomasi, J. Approximate Evaluations of the Electrostatic Free Energy and Internal Energy Changes in Solution Processes. *Chem. Phys.* **1982**, *65*, 239–245. [CrossRef]
27. Pascual-Ahuir, J.; Silla, E.; Tuñon, I. GEPOL: An Improved Description of Molecular Surfaces. III. A New Algorithm for the Computation of a Solvent-excluding Surface. *J. Comput. Chem.* **1994**, *15*, 1127–1138. [CrossRef]
28. Kadhim, A.; Betti, N.; Al-Bahrani, H.A.; Al-Ghezi, M.K.S.; Gaaz, T.; Kadhum, A.H.; Alamiery, A. A Mini Review on Corrosion, Inhibitors and Mechanism Types of Mild Steel Inhibition in an Acidic Environment. *Int. J. Corros. Scale Inhib.* **2021**, *10*, 861–884. [CrossRef]
29. Perdew, J.; Parr, R.; Levy, M.; Balduz, J. Density-Functional Theory for Fractional Particle Number: Derivative Discontinuities of the Energy. *Phys. Rev. Lett.* **1982**, *49*, 1691–1694. [CrossRef]
30. Pearson, R. Absolute Electronegativity and Hardness: Application to Inorganic Chemistry. *Inorg. Chem.* **1988**, *27*, 734–740. [CrossRef]
31. Gazquez, J. A Hardness and Softness Theory of Bond Energies and Chemical Reactivity. *Theor. Org. Chem.* **1998**, *5*, 135–152. [CrossRef]
32. Chattaraj, P.; Sarkar, U.; Roy, D. Electrophilicity Index. *Chem. Rev.* **2006**, *106*, 2065–2091. [CrossRef]
33. Gazquez, J.; Cedillo, A.; Vela, A. Electrodonating and Electroaccepting Powers. *J. Phys. Chem.* **2007**, *111*, 1966–1970. [CrossRef] [PubMed]
34. Momma, K.; Izumi, F. VESTA 3 for Three-Dimensional Visualization of Crystal, Volumetric and Morphology Data. *J. Appl. Crystallogr.* **2011**, *44*, 1272–1276. [CrossRef]
35. Elstner, M.; Porezag, D.; Jungnickel, G.; Elsner, J.; Haugk, M.; Frauenheim, T.; Suhai, S.; Sifert, G. Self-Consistent-Charge Density-Functional Tight-Binding Method for Simulations of Complex Materials Properties. *Phys. Rev. B* **1998**, *58*, 7260–7268. [CrossRef]

36. Niehaus, T.; Elstner, M.; Frauenheim, T.; Suhai, S. Application of an Approximate Density-Functional Method to Sulfur Containing Compounds. *J. Mol. Struct. Theochem.* **2001**, *541*, 185–194. [CrossRef]
37. Gaus, M.; Cui, Q.; Elstner, M. DFTB3: Extension of the Self-Consistent-Charge Density-Functional Tight-Binding Method (SCC-DFTB). *J. Chem. Theory Comput.* **2011**, *7*, 931–948. [CrossRef]
38. Zheng, G.; Witek, H.; Bobadova-Parvanova, P.; Irle, S.; Musaev, D.; Prabhakar, R.; Morokuma, K.; Lundberg, M.; Elstner, M.; Köhler, C.; et al. Parameter Calibration of Transition-Metal Elements for the Spin-Polartaed Self-Consistent-Charge Density-Functional Tight-Binding (DFTB) Method: Sc, Ti, Fe, Co, and Ni. *J. Chem. Theory Comput.* **2007**, *3*, 1349–1367. [CrossRef]
39. Tshikhudo, F.; Mugwena, D.; Mnyakeni-Moleele, S.; Kabanda, M.; Fernandez, C.; Murulana, L. Synthesis of Substituted Triazines and Evaluation of Their Corrosion Inhibition Performance on Fe(100) in 1 M HCl: A Combined Experimental and DFT Study. *Int. J. Electrochem. Sci.* **2025**, *20*, 101153. [CrossRef]
40. Balasooriya, H.; Li, C.; Wang, F. Understanding Steel Corrosion: Surface Chemistry and Defects Explored Through DFT Modelling—A Review. *Processes* **2025**, *13*, 1971. [CrossRef]
41. Boudalia, M.; Fernández-Domene, R.; Guo, L.; Echihi, S.; Belghiti, M.; Zarrouk, A.; Bellaouchou, A.; Guenbour, A.; García-Antón, J. Experimental and Theoretical Tests on the Corrosion Protection of Mild Steel in Hydrochloric Acid Environment by the Use of Pyrazole Derivative. *Materials* **2023**, *16*, 678. [CrossRef]
42. Meng, S.; Liu, Z.; Zhao, X.; Fan, B.; Liu, H.; Guo, M.; Hao, H. Efficient Corrosion Inhibition by Sugarcane Purple Rind Extract for Carbon Steel in HCl Solution: Mechanism Analyses by Experimental and: In Silico Insights. *RSC Adv.* **2021**, *11*, 31693–31711. [CrossRef] [PubMed]
43. Abdulazeez, I.; Zeino, A.; Kee, C.; Al-Saadi, A.; Khaled, M.; Wong, M.; Al-Sunaidi, A. Mechanistic Studies of the Influence of Halogen Substituents on the Corrosion Inhibitive Efficiency of Selected Imidazole Molecules: A Synergistic Computational and Experimental Approach. *Appl. Surf. Sci.* **2019**, *471*, 494–505. [CrossRef]
44. El, F.; Salim, R.; Taleb, M.; Benhiba, F.; Rezki, N.; Chauhan, D.; Quraishi, M. Pyridinium-Based Ionic Liquids as Novel Eco-Friendly Corrosion Inhibitors for Mild Steel in Molar Hydrochloric Acid: Experimental & Computational Approach. *Surf. Interfaces* **2021**, *22*, 100881. [CrossRef]
45. Humphrey, W.; Dalke, A.; Schulten, K. VMD: Visual Molecular Dynamics. *J. Mol. Graph.* **1996**, *14*, 33–38. [CrossRef] [PubMed]
46. Soler, J.M.; Artacho, E.; Gale, J.D.; García, A.; Junquera, J.; Ordejón, P.; Sánchez-Portal, D. The SIESTA Method for Ab Initio Order-N Materials Simulation. *J. Phys. Condens. Matter* **2002**, *14*, 2745–2779. [CrossRef]
47. García, A.; Papior, N.; Akhtar, A.; Artacho, E.; Blum, V.; Bosoni, E.; Brandimarte, P.; Brandbyge, M.; Cerdá, J.I.; Corsetti, F.; et al. Siesta: Recent Developments and Applications. *J. Chem. Phys.* **2020**, *152*, 204108. [CrossRef]
48. Perdew, J.P.; Burke, K.; Ernzerhof, M. Generalized Gradient Approximation Made Simple. *Phys. Rev. Lett.* **1996**, *77*, 3865, Erratum in *Phys. Rev. Lett.* **1997**, *78*, 1396. https://doi.org/10.1103/PhysRevLett.78.1396. [CrossRef]
49. Louwerse, M.J.; Rothenberg, G. Transferable Basis Sets of Numerical Atomic Orbitals. *Phys. Rev. B—Condens. Matter Mater. Phys.* **2012**, *85*, 035108. [CrossRef]
50. Batatia, I.; Kovács, D.P.; Simm, G.N.C.; Ortner, C.; Csányi, G. MACE: Higher Order Equivariant Message Passing Neural Networks for Fast and Accurate Force Fields. In *Advances in Neural Information Processing Systems 35 (NeurIPS 2022)*; Neural Information Processing Systems Foundation, Inc. (NeurIPS): San Diego, CA, USA, 2022.
51. Batatia, I.; Benner, P.; Chiang, Y.; Elena, A.M.; Kovács, D.P.; Riebesell, J.; Advincula, X.R.; Asta, M.; Avaylon, M.; Baldwin, W.J.; et al. A Foundation Model for Atomistic Materials Chemistry. *J. Chem. Phys.* **2025**, *163*, 184110. [CrossRef]
52. Larsen, A.H.; Mortensen, J.J.; Blomqvist, J.; Castelli, I.E.; Christensen, R.; Dułak, M.; Friis, J.; Groves, M.N.; Hammer, B.; Hargus, C.; et al. The Atomic Simulation Environment—A Python Library for Working with Atoms. *J. Phys. Condens. Matter* **2017**, *29*, 273002. [CrossRef]
53. Jeschke, S.; Wilson, K.; Lee, A.F. Accelerating Computational Modeling of Reactant Adsorption through a Combined MACE + DFT Approach: Furfural on Cu Surfaces. *J. Phys. Chem. C* **2025**, *129*, 11948–11957. [CrossRef]
54. Calderan, F.V.; Andriani, K.F.; Felício-Sousa, P.; Pinheiro, G.A.; Da Silva, J.L.F.; Quiles, M.G. Cut-SOAP: A Machine Learning Descriptor for Rapid Screening of Molecular Adsorption Energetics. *ACS Omega* **2026**, *11*, 7948–7958. [CrossRef]
55. Mathanker, A.; Guo, J.; Goldsmith, B.R.; Varley, J.B.; Govindarajan, N. Estimating Potential-Dependent Physicochemical Properties at Metal−Electrolyte Interfaces Using Machine Learning Interatomic Potentials. *ACS Electrochem.* **2026**, *2*, 1176–1189. [CrossRef]
56. Ouakki, M.; Galai, M.; Rbaa, M.; Abousalem, A.; Lakhrissi, B.; Rifi, E.; Cherkaoui, M. Quantum Chemical and Experimental Evaluation of the Inhibitory Action of Two Imidazole Derivatives on Mild Steel Corrosion in Sulphuric Acid Medium. *Heliyon* **2019**, *5*, e02759. [CrossRef] [PubMed]
57. Kedimar, N.; Rao, P.; Rao, S. Imidazole-Based Ionic Liquid as Sustainable Green Inhibitor for Corrosion Control of Steel Alloys: A Review. *J. Mol. Liq.* **2024**, *411*, 125789. [CrossRef]
58. Choudhary, V.; Saini, N.; Prakashaiah, B.; Khatri, P.; Jain, S.; Bisht, Y.; Khan, T. Performance Evaluation of Amino Acid-Based Ionic Liquids as Corrosion Inhibitors for Mild Steel: Synthesis, Electrochemical, Gravimetric, and Theoretical Aspects. *Next Mater.* **2025**, *8*, 100587. [CrossRef]

59. Obot, I.; Obi-Egbedi, N. Adsorption Properties and Inhibition of Mild Steel Corrosion in Sulphuric Acid Solution by Ketoconazole: Experimental and Theoretical Investigation. *Corros. Sci.* **2010**, *52*, 198–204. [CrossRef]
60. Ouakki, M.; Rbaa, M.; Galai, M.; Lakhrissi, B.; Rifi, E.; Cherkaoui, M. Experimental and Quantum Chemical Investigation of Imidazole Derivatives as Corrosion Inhibitors on Mild Steel in 1.0 M Hydrochloric Acid. *J. Bio-Tribo-Corros.* **2018**, *4*, 35. [CrossRef]
61. Vidyashree, G.; Manjunatha, K.; Devendra, B.; Shweta, M.; Poojary, L.; Praveen, M.; Rathod, M.; Sunil, K.; Talawar, V. Synthesis, Characterization and Corrosion Inhibition Evaluation of a New Chalcone Derivative 2-3-(3-Hydroxyphenyl)-1-[4-(1H-Imidazol-1-Yl) Phenyl] Prop-2-En-1-One for Mild Steel Corrosion in 1M HCl Assessment with DFT and MD Studies. *Results Surf. Interfaces* **2024**, *17*, 100336. [CrossRef]
62. Báez-Castro, A.; Baldenebro-López, J.; Glossman-Mitnik, D.; Höpfl, H.; Cruz-Enríquez, A.; Miranda-Soto, V.; Parra-Hake, M.; Campos-Gaxiola, J.J. Novel Synthesis, Structural Analysis, Photophysical Properties and Theoretical Study of 2,4,5-Tris(2-Pyridyl)Imidazole. *J. Mol. Struct.* **2015**, *1099*, 126–134. [CrossRef]
63. Felaly, R.N.; Abdallah, M.; Al-Gorair, A.S.; Hawsawi, H.; Al-Juaid, S.S.; Sobhi, M.; El Wanees, S.A.; Zarrouk, A.; Soliman, K.A. Experimental and Computational Evaluation of Expired Anticonvulsant Drugs as Corrosion Inhibitors for 316 Stainless Steel in HCl Solutions. *Int. J. Electrochem. Sci.* **2026**, *21*, 101264. [CrossRef]
64. Nahlé, A.; Salim, R.; Hajjaji, F.; Ech-chihbi, E.; Titi, A.; Messali, M.; Kaya, S.; IBrahimi, B.; Taleb, M. Experimental and Theoretical Approach for Novel Imidazolium Ionic Liquids as Smart Corrosion Inhibitors for Mild Steel in 1.0 M Hydrochloric Acid. *Arab. J. Chem.* **2022**, *15*, 103967. [CrossRef]
65. Delgado-Montiel, T.; Baldenebro-López, J.; Soto-Rojo, R.; Glossman-Mitnik, D. Theoretical Study of the Effect of π-Bridge on Optical and Electronic Properties of Carbazole-Based Sensitizers for DSSCs. *Molecules* **2020**, *25*, 3670. [CrossRef]
66. Khadom, A.; Mahmmod, A. Quantum Chemical and Mathematical Statistical Calculations of Phenyltetrazole Derivatives as Corrosion Inhibitors for Mild Steel in Acidic Solution: A Theoretical Approach. *Results Eng.* **2022**, *16*, 100741. [CrossRef]
67. Flores-Frías, E.; Martínez-Valencia, H.; Barba-López, V.; Baldenebro-López, J.; Landeros-Martinez, L. Electrochemical and Computational Study of the Epicatechin-3-Gallate Isolated from Green Tea Leaves as a Corrosion Inhibitor for 1018 Carbon Steel in Sulfuric Acid. *Int. J. Electrochem. Sci.* **2025**, *20*, 101092. [CrossRef]
68. Feng, L.; Yang, H.; Wang, F. Experimental and Theoretical Studies for Corrosion Inhibition of Carbon Steel by Imidazoline Derivative in 5% NaCl Saturated $Ca(OH)_2$ Solution. *Electrochim. Acta* **2011**, *58*, 427–436. [CrossRef]
69. Kolasinski, K. *Surface Science: Foundations of Catalysis and Nanoscience*, 2nd ed.; WILEY: Hoboken, NJ, USA, 2012.
70. Bondi, A. Van Der Waals Volumes and Radii. *J. Phys. Chem.* **1964**, *68*, 441. [CrossRef]
71. Alvarez, S. A Cartography of the van Der Waals Territories. *Dalton Trans.* **2013**, *42*, 8617–8636. [CrossRef] [PubMed]